The Astrophysical Journal, 811:81 (12pp), 2015 October 1 doi:10.1088/0004-637X/811/2/81

THE FORMATION OF *IRIS* DIAGNOSTICS. VI. THE DIAGNOSTIC POTENTIAL OF THE C II LINES AT 133.5 nm IN THE SOLAR ATMOSPHERE

Bhavna Rathore[1], Mats Carlsson[1], Jorrit Leenaarts[2], and Bart De Pontieu[1,3]
[1] Institute of Theoretical Astrophysics, University of Oslo, P.O. Box 1029 Blindern, NO-0315 Oslo, Norway; bhavna.rathore@astro.uio.no, mats.carlsson@astro.uio.no, bdp@lmsal.com
[2] The Institute for Solar Physics, AlbaNova University Center, SE-106 91 Stockholm, Sweden; jorrit.leenaarts@astro.su.se
[3] Lockheed Martin Solar & Astrophysics Lab, Org. A021S, Bldg. 252, 3251 Hanover Street Palo Alto, CA 94304, USA
Received 2015 June 5; accepted 2015 August 17; published 2015 September 24

ABSTRACT

We use 3D radiation magnetohydrodynamic models to investigate how the thermodynamic quantities in the simulation are encoded in observable quantities, thus exploring the diagnostic potential of the C II 133.5 nm lines. We find that the line core intensity is correlated with the temperature at the formation height but the correlation is rather weak, especially when the lines are strong. The line core Doppler shift is a good measure of the line-of-sight velocity at the formation height. The line width is both dependent on the width of the absorption profile (thermal and non-thermal width) and an opacity broadening factor of 1.2–4 due to the optically thick line formation with a larger broadening for double peak profiles. The C II 133.5 nm lines can be formed both higher and lower than the core of the Mg II k line depending on the amount of plasma in the 14–50 kK temperature range. More plasma in this temperature range gives a higher C II 133.5 nm formation height relative to the Mg II k line core. The synthetic line profiles have been compared with *Interface Region Imaging Spectrograph* observations. The derived parameters from the simulated line profiles cover the parameter range seen in observations but, on average, the synthetic profiles are too narrow. We interpret this discrepancy as a combination of a lack of plasma at chromospheric temperatures in the simulation box and too small non-thermal velocities. The large differences in the distribution of properties between the synthetic profiles and the observed ones show that the C II 133.5 nm lines are powerful diagnostics of the upper chromosphere and lower transition region.

Key words: radiative transfer – Sun: atmosphere – Sun: chromosphere – Sun: transition region – Sun: UV radiation

1. INTRODUCTION

This is the second paper in the series exploring the diagnostic potential of the C II lines around 133.5 nm under solar conditions. There are three components in the multiplet: at 133.4532 nm, hereafter called the C II 133.4 nm line, and at 133.5708 nm with a weaker blend at 133.5663 nm, hereafter together called the C II 133.5 nm line. These lines are among the strongest lines in the far-ultraviolet (FUV) range of NASA's *Interface Region Imaging Spectrograph* (*IRIS*) space mission and exploring their diagnostic potential is therefore of great interest. In Rathore & Carlsson (2015; hereafter called Paper I), we analyzed the basic rate balance under solar chromospheric conditions and showed that a nine-level model atom sufficed to describe the ionization and excitation balance for the proper modeling of the C II lines around 133.5 nm. We also studied the general formation processes in Paper I and found that the lines are mainly formed in the optically thick regime with an average formation temperature of 10 kK and a line core formation close to a column mass of 10^{-6} g cm^{-2}.

For references to earlier work on these C II lines, we refer to Paper I. Here, we will focus on the diagnostic potential of the C II lines and explore correlations between observable quantities and properties of a snapshot from a 3D MHD model calculated with the *Bifrost* code (Gudiksen et al. 2011). We will also compare the synthetic observables with observations from *IRIS* to determine the applicability of the deduced relations.

The organization of this paper is as follows. In Section 2, we describe the radiative transfer code used. In Section 3, we present the snapshot from the 3D MHD simulation. In Section 4, we present the synthetic spectra and discuss line profiles, how to define the line core and formation heights. In Section 5, we discuss the diagnostic potential of the lines. We compare with other spectral lines in the *IRIS* passbands in Section 6 and with *IRIS* observations in Section 7. We summarize and add concluding remarks in Section 8.

2. RADIATIVE TRANSFER

In the present work, we have used the full 3D radiative transfer code MULTI3D (Leenaarts & Carlsson 2009), and the same nine-level quintessential atomic model for C II arrived at in Paper I. The MULTI3D code solves the coupled statistical equilibrium and radiative transfer equations in full 3D. For our computations, we assume complete frequency redistribution (CRD), an approximation that was shown to be adequate in Paper I. The blend between the 133.5708 and 133.5663 nm lines is taken into account self-consistently as are the overlaps between the C I photoionization continua (Rybicki & Hummer 1991, 1992). The code includes the local approximate operator of Olson et al. (1986), Ng acceleration (Ng 1974), collisional-radiative switching (Hummer & Voels 1988), and background opacities from the Uppsala Opacity Package (Gustafsson 1973).

3. MODEL ATMOSPHERE

To explore relations between observable quantities and atmospheric quantities, we have used a 3D snapshot from the simulation *en024048_hion* calculated with the 3D radiative magnetohydrodynamic (RMHD) code *Bifrost* (Gudiksen et al. 2011). We use the simulation snapshot 385, the same as has been used in previous papers on the formation of *IRIS* diagnostics (Leenaarts et al. 2013a, 2013b; Pereira et al.

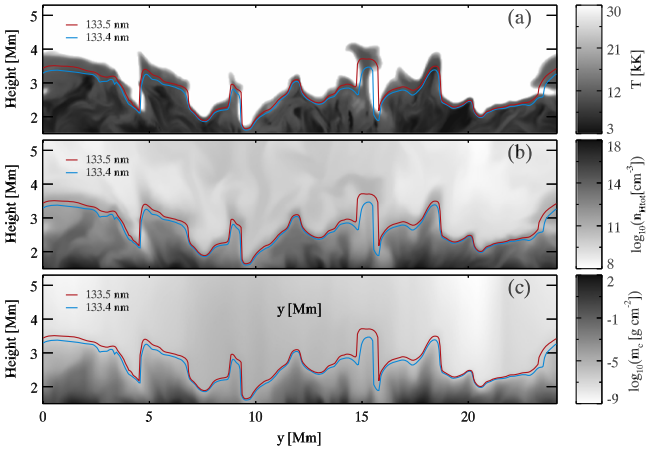

Figure 1. Temperature (a), total hydrogen population density (b), and column mass (c) as a function of height along a 2D cutout at $x = 12$ Mm from the 3D model atmosphere. The maximum height across the line profile of $\tau_\nu = 1$ is shown for the C II 133.5 nm (red) and C II 133.4 nm (blue) lines.

2013, 2015) and a number of other papers on line formation under solar chromospheric conditions (Leenaarts et al. 2012; Štěpán et al. 2012; de la Cruz Rodríguez et al. 2013). The full simulation cubes with all variables as a function of grid position are available from the European Hinode Science Data Centre (http://www.sdc.uio.no/search/simulations). A detailed description of the simulation *en024048_hion* is given in Carlsson et al. (2015) and we summarize some of the properties below.

The simulation box is $24 \times 24 \times 16.8$ Mm^3 discretized onto $504 \times 504 \times 496$ grid points. The vertical extent is from 2.4 Mm below to 14.4 Mm above the photosphere and covers the upper convection zone, photosphere, chromosphere, and lower corona. The horizontal grid is equidistant with 48 km spacing and periodic boundaries. Vertically, the grid spacing is 19 km from $z = -1$ Mm up to $z = 5$ Mm. The spacing increases toward the lower and upper boundaries to a maximum of 98 km at the coronal boundary. The magnetic field was introduced into the computational box as two opposite polarity blobs separated by 8 Mm. This large-scale structure is evident throughout the simulation, though a lot of small-scale structure develops from the action of the convection on the magnetic field. The mean unsigned field strength is 50 G in the photosphere.

We illustrate the simulation box by showing a cut at $x = 12$ Mm in Figure 1. The figure shows the temperature, the total hydrogen population density, and the column mass as functions of height and position along the y-coordinate in the simulation box. The figure shows the line core height of unit optical depth of both the C II lines as red and blue lines. At this line core formation height, we have a temperature in the range of 9–14 kK, the density is of the order of 10^{-14}–10^{-12} g cm^{-3}, the total hydrogen particle density is 10^9–10^{12} cm^{-3}, and the column mass is of order 10^{-6} g cm^{-2}.

4. BASIC CHARACTERISTICS

4.1. Line Profiles

From this simulation, we get a very broad range of intensities and shapes of the line profiles. The line profiles can have a single peak, double peaks, three peaks and even be in absorption. Some typical line profiles are shown in Figure 2.

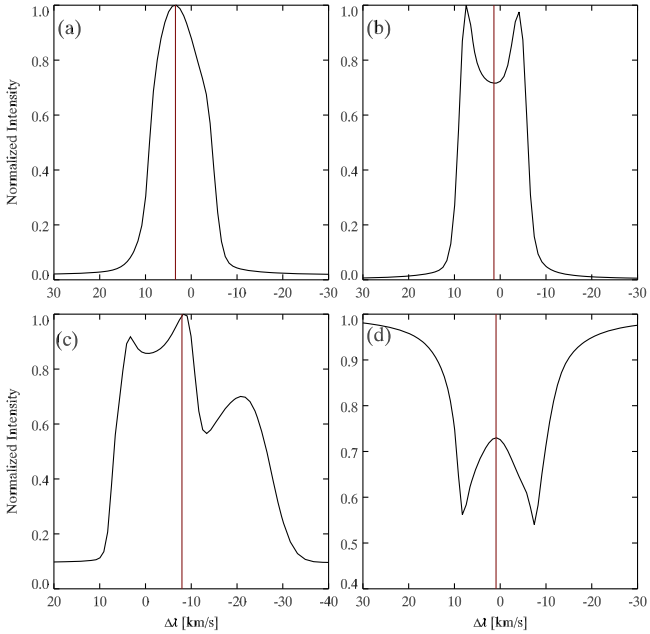

Figure 2. Various C II line profiles from our simulation with the position of the line center using our peak finding algorithm shown with a red vertical line: typical single-peak emission line profile (a), double-peak profile with central depression (b), profile showing three peaks (c), and absorption line profile (d).

We show these line profiles and make all our subsequent analyses at the full resolution of the simulation, without smearing the profiles to *IRIS* resolution. We will discuss the effects of the *IRIS* resolution on the results in Section 8.

The diversity of intensity profiles is the result of the interplay between the source function and the optical depth variation along the line of sight. Single-peak profiles result from source functions that increase monotonically with height up to the height where the line core has optical depth unity. We get a double peak when the source function has a local maximum and then decreases before the height of optical depth unity in the line core. We may get more peaks when we have source functions with multiple local maxima. This scenario is further complicated by velocity gradients that Doppler shift the maximum of the local absorption profile. These velocity gradients may partly smear out an otherwise symmetric double-peak profile rendering it single-peak, but asymmetric, with the intensity maximum on the red or blue side of the line core.

The number of peaks varies between the lines. The C II 133.4 nm line has more single-peak profiles than the C II 133.5 nm line (see Figure 3). The explanation is that the C II 133.5 nm is the stronger of the two main components of the multiplet so the optical depth unity point is higher up in the atmosphere (see also Figure 1). There is thus a higher probability that the line core is formed above the height where the source function has a local maximum, thus causing a central reversal (i.e., double-peak profile) more easily for the C II 133.5 nm line.

4.2. Defining the Line Core

Diagnostics derived from a given wavelength in the line, e.g., the line core, can be expected to give information from a narrow region of the atmosphere compared with diagnostics derived from the full line profile, e.g., moments of the intensity or parameters from a Gaussian fit. In Paper I, we defined the

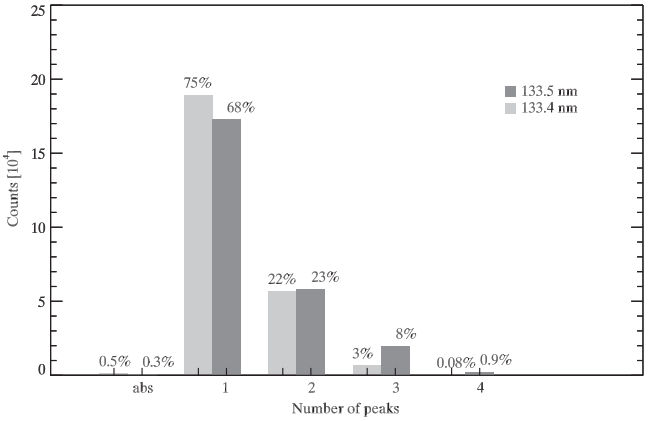

Figure 3. Statistics of number of intensity peaks in the C II 133.4 nm and C II 133.5 nm lines in the 3D snapshot.

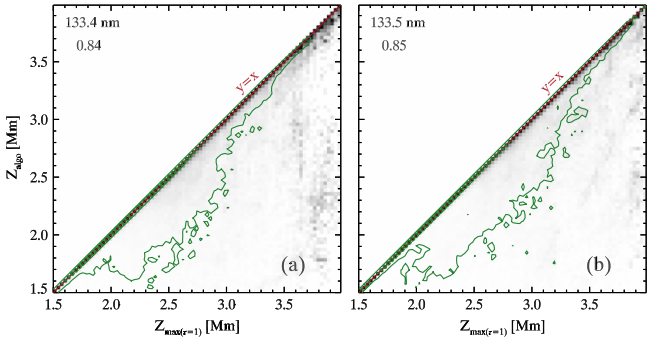

Figure 4. Probability distribution function (PDF) of $\tau = 1$ height at the line center determined by the line center finding algorithm as a function of the theoretical line core $\tau = 1$ height (the maximum $\tau = 1$ height over the line profile) for the C II 133.4 nm line (a) and the C II 133.5 nm line (b). Each column in the panels is scaled to maximum contrast to increase visibility. The inner green contour encompasses 50% and the outer contour encompasses 90% of all points. The red line denotes $y = x$. The Pearson correlation coefficient is given in the upper left corner.

line core as the wavelength where the height at which optical depth reaches unity is maximal. This is a reasonable definition from a theoretical point of view but it is not practical observationally since the optical depths are not known.

In an attempt to get a good observational definition of the line core, we have made an algorithm to pick the position of the line core for all kinds of line profiles. To extract the line center position, we consider the profile within the spectral range of $(-50 < \Delta v < 50\,\mathrm{km\,s^{-1}})$ around the rest wavelength of each line. We define the line core on the basis of the number of maxima and minima in the line profile. For single-peak profiles, the line core is simply defined to be at the central maximum. For double-peak profiles, the line core is defined to be at the minimum between the two maxima. For three peak profiles, the line core is defined to be at the maximum between the two minima. Similarly, for an even number of peaks, the line core is defined to be at the central minimum and for an odd number of peaks, the line core is defined to be at the central maximum. A similar procedure is adopted for absorption profiles. Line centers according to this algorithm are shown in Figure 2. To avoid small peaks close to the continuum intensity, we only consider the line profile with an intensity 50% above the continuum. For real observations, care must be taken not to count maxima caused by noisy data. This can be achieved by first applying smoothing or noise filtering (e.g., Wiener filtering) to the data.

Figure 4 shows the relation between the theoretical line core optical depth unity height (the maximum $\tau_\nu = 1$ height over the line profile) and the height of $\tau_\nu = 1$ at the wavelength of the line center determined with our algorithm. For a majority of the profiles, the algorithm works well in finding the same wavelength as the theoretical line core, but there are some cases where the observationally found line center is quite different from the theoretical one, resulting in a large difference between the heights. This may happen when effects of large velocity gradients smear out local minima such that a profile that would exhibit two peaks in the absence of velocity fields appears single peaked and rather asymmetric. Our algorithm then picks out the intensity maximum, which can be some distance away from the theoretical line core. For 75% of the columns in the 3D model, the difference between the two heights is less than 100 km while for 5% of the columns, the difference is larger than 1 Mm.

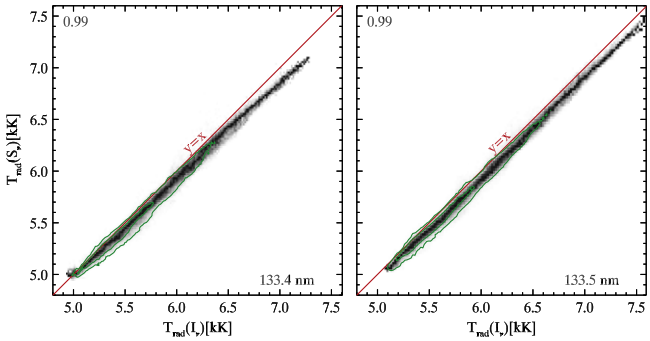

Figure 5. PDF of the radiation temperature of the source function at the $\tau_\nu = 1$ height as a function of the radiation temperature of the intensity. The correlation is shown for the theoretical line core (the wavelength where the height where optical depth unity is the maximum). Each column in the panels is scaled to maximum contrast to increase visibility. The green contours encompass 50% and 90% of all points. The Pearson correlation coefficient is given in the upper left corner, the red line denotes $y = x$.

4.3. Formation Height

For optically thick line formation, the Eddington–Barbier relation often gives a good indication of where the intensity comes from. The Eddington–Barbier relation states that the disk center outgoing intensity is approximately equal to the source function at optical depth unity. This relation is exact if the source function is a linear function of optical depth, but is often a good approximation also when the source function is quite nonlinear (which is normally the case in the ultraviolet part of the spectrum where the Planck function is close to an exponential function of temperature).

Figure 5 shows the correlation between the line intensity at the theoretical line core (see Section 4.2) and the source function at the $\tau_\nu = 1$ height. The correlation is quite good, especially for the lower intensity values. The higher intensities correspond to columns where the source function at optical depth unity is high. These columns often show a steep source function rise with height and therefore an average contribution shifted toward optical depths smaller than unity where the source function is higher.

Figure 5 tells us that optical depth unity is a good first approximation to the formation height except for columns with a steep, nonlinear, temperature gradient, where optical depth

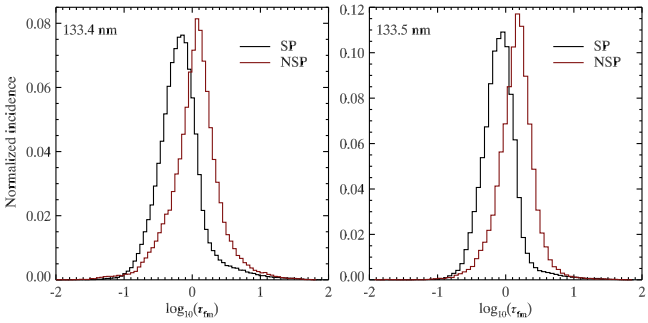

Figure 6. Histogram of average formation height on a $\lg(\tau_0)$ scale (see Equation (4)) for single-peak (SP; black) and non-single-peak (NSP, red) profiles for the C II 133.4 nm line (left) and the C II 133.5 nm line (right).

unity gives too low heights (and too low formation temperatures). Instead of using a one-point integration formula for the relation between the source function and the outgoing intensity (like the Eddington–Barbier relation), we may use the formal solution to the transfer equation to define the contribution function to intensity at solar disk center, $C_{I_\nu}(z)$:

$$C_{I_\nu}(z) = S_\nu(z) e^{-\tau_\nu(z)} \chi_\nu(z), \tag{1}$$

where S_ν is the source function, χ_ν is the extinction coefficient, and τ_ν is the optical depth at frequency ν, with all of these quantities as functions of height, z.

The C II lines are mainly formed in the optically thick regime. However, we may have a substantial optically thin component to the intensity in the cases where the source function rises rapidly with height, as seen in Figure 5. There are also cases among the low-intensity profiles where this is the case, as also exemplified in Paper I. To further quantify the relative importance of the optically thin and thick contributions, we use the contribution function to the total intensity:

$$C_{I_{\rm total}}(z) = \int C_{I_\nu}(z)\, d\nu. \tag{2}$$

The contribution to total intensity on a $\lg\tau_0$ scale (lg denotes the logarithm to the base of 10) is obtained from

$$C_{I_{\rm total}}(\lg\tau_0) = C_{I_{\rm total}}(z) \frac{dz}{d\lg\tau_0}, \tag{3}$$

where τ_0 is the optical depth at the line core.

We also define the mean formation depth in $\lg\tau_0$ from

$$\lg\tau_{\rm fm} = \frac{\int \lg\tau_0\, C_{I_{\rm total}}(\lg\tau_0)\, d\lg\tau_0}{\int C_{I_{\rm total}}(\lg\tau_0) d\lg\tau_0}. \tag{4}$$

If we have a substantial thin contribution to the total intensity, we expect the mean formation depth to be at an optical depth significantly smaller than one. Figure 6 shows a histogram of the formation depth in lg τ_0 for all of the columns in the simulation box. We show histograms separately for single-peak profiles and the other profiles. For non-single-peak profiles, we have a distribution that is centered on $\lg\tau_{\rm fm} = 0 - 0.2$ while single-peak profiles show distributions skewed to smaller optical depths. This clearly shows the effect of a steep nonlinear source function rising toward smaller optical depths. However, there are very few columns where the formation could be described as being dominated by a very thin contribution.

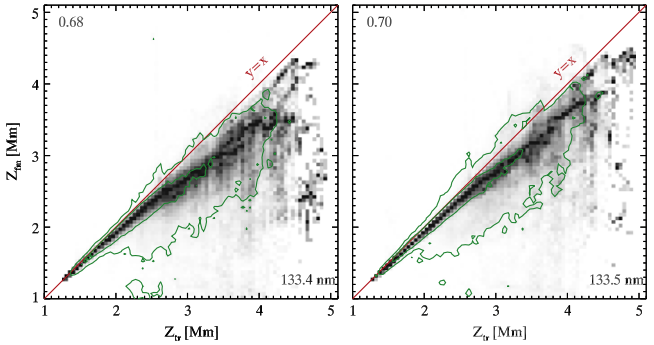

Figure 7. PDF of formation height as a function of transition region height (defined to be the lowest height in a column where the temperature is greater than 30 kK) for the C II 133.4 nm line (left) and the C II 133.5 nm line (right). Each column in the panels is scaled to maximum contrast to increase visibility. The green contours encompass 50% and 90% of all points. The Pearson correlation coefficient is given in the upper left corner, the red line denotes $y = x$.

We now turn to describing the formation height relative to the height of the transition region. We define the formation height $Z_{\rm fm}$ from the contribution function weighted average height:

$$Z_{\rm fm}(\nu) = \frac{\int z\, C_{I_\nu}(z)\, dz}{\int C_{I_\nu}(z)\, dz}. \tag{5}$$

Figure 7 shows the relation between the transition region height and this formation height for the theoretical line core wavelength for the C II 133.4 nm and C II 133.5 nm lines. The transition region height is defined as the lowest height where the temperature is greater than 30 kK. Both lines are formed just below this transition region height. The difference in height is larger when the transition region is higher in the atmosphere. The formation height is very close to the transition region when the transition region is very low in the atmosphere. This corresponds to locations of strong flux concentrations in the photosphere.

5. DIAGNOSTIC POTENTIAL

In Paper I and in Section 4, we established the basic formation characteristics of the C II lines. In this section, we will correlate observables with the hydrodynamical state in the simulation in order to explore the diagnostic potential of the C II lines. The figures are organized with the observable quantity along the x axis and the atmospheric property along the y axis. We normally show the probability density function (PDF) of the atmospheric quantity as a function of the observed quantity normalized by column to bring out the correlation also where there are few points. What appears as a bad correlation at the extreme ranges may thus affect only a small number of cases. Contours are therefore added that encompass 50% and 90% of the points in the simulation. We start by looking at the intensity, continue with line shifts and finish by looking at the line widths.

5.1. Intensity

5.1.1. Versus Formation Height

Figure 8 shows the correlation between line core intensity and formation height. The low intensity profiles tend to have a

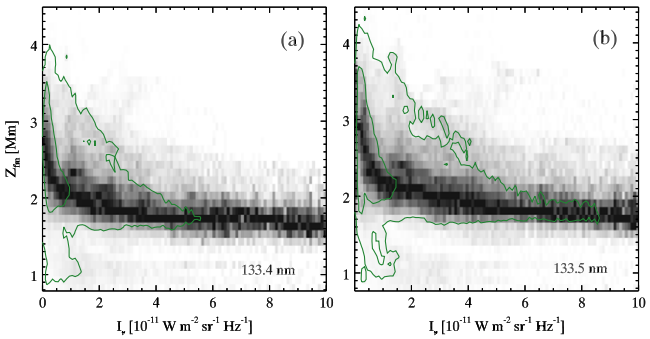

Figure 8. PDF of formation height (see Section 4.3 and Equation (5)) as a function of intensity at the line core for C II 133.4 nm (left panel) and C II 133.5 nm (right panel). Each column in the panels is scaled to maximum contrast to increase visibility. The green contours encompass 50% and 90% of all points.

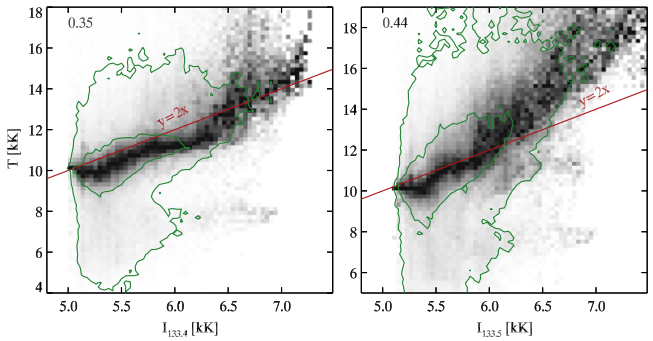

Figure 9. PDF of the temperature at the formation height as a function of the radiation temperature of the intensity at the line core for the C II 133.4 nm line (left panel) and the C II 133.5 nm line (right panel). Each column in the panels is scaled to maximum contrast to increase visibility. The green contours encompass 50% and 90% of all points. The Pearson correlation coefficient is given in the upper left corner of both panels. The red line denotes the line $y = 2x$.

higher formation height. Since low intensity means low source function at the formation height (Figure 5) and the lines are formed close to the transition region (Figure 7), the relation shown in Figure 8 thus means that the source function is low when the transition region is at a large height.

5.1.2. Versus Temperature

The line core intensity is closely correlated with the source function at optical depth unity (Figure 5), but how does the source function relate to the temperature? With a close coupling between the Planck function and the source function, we could use the intensity as a probe of the temperature at the height of formation. Figure 9 shows the correlation between the radiation temperature of the line core intensity and the temperature at the formation height. We find that the temperature at the formation height of the line is approximately twice the radiation temperature of the line core intensity of both the lines. This means that the source function has decoupled from the Planck function at the formation height and the amount of decoupling varies quite a bit, causing a large scatter and a small correlation coefficient. Inspection of the corresponding images of radiation temperature of the core intensity and temperature at the formation height also shows that the spread is too large for the weak correlation to be of practical use.

5.1.3. Line Ratio

The intensity ratio between the C II 133.5 nm and the C II 133.4 nm lines is 1.8 in the optically thin case and can be any value in the optically thick case depending on the ratio of the source functions of the two lines (see Paper I). Figure 10 shows a histogram of this ratio in the *Bifrost* simulation. The peak intensity ratio is around 1.7 for single-peak profiles and 1.4 for the peaks of double-peak profiles. The double peaks are formed lower in the atmosphere than the single peaks and because of the higher density, we expect the source functions to be more equal leading to a smaller ratio. In addition, the peak intensity for double-peak profiles is formed at the local source function maximum, which is typically at the same height for both lines. We therefore have no effect of different formation heights for double-peak profiles, while for single-peak profiles the C II 133.5 nm intensity is formed higher in the atmosphere than the C II 133.4 nm intensity. There, the source function is higher, thus also leading to a higher line ratio.

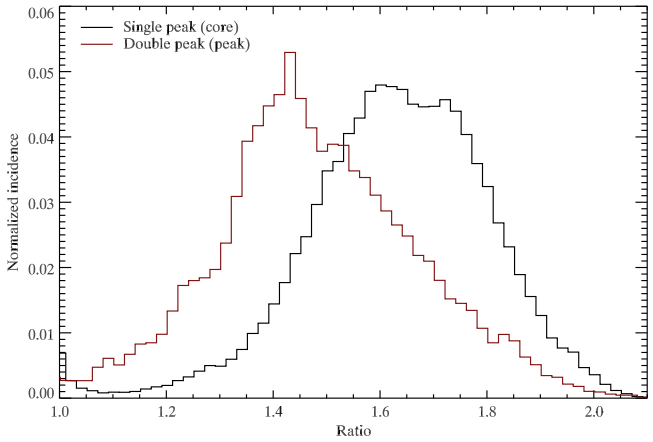

Figure 10. Histogram of the line peak intensity ratio of single-peak (black) and double-peak (red) profiles from the simulation.

5.1.4. Line Asymmetry

Double-peak profiles often show an asymmetry with one peak brighter than the other. For the Mg II h and k lines, Leenaarts et al. (2013b) showed that the asymmetry is caused by a velocity gradient between the heights of formation of the peaks and the line core. We define an asymmetry measure as

$$R_c = \frac{I_b - I_r}{I_b + I_r}, \tag{6}$$

where I_b is the blue peak intensity and I_r is the red peak intensity. R_c is thus positive if the blue peak is stronger and negative if the red peak is stronger.

We furthermore define the velocity difference between the core and peak formation heights from

$$v_{\rm diff} = v(z_0) - v(z_p), \tag{7}$$

where $v(z_p)$ is the velocity at the average of the heights of optical depth unity for the blue and the red peak and $v(z_0)$ is the velocity at the height of optical depth unity for the line core. Positive velocity is upflow.

Figure 11 shows how this asymmetry measure is correlated with the velocity difference defined above. A blue peak that is stronger than the red peak (positive R_c) is correlated with a downflow of matter (relative to the velocity at the peak

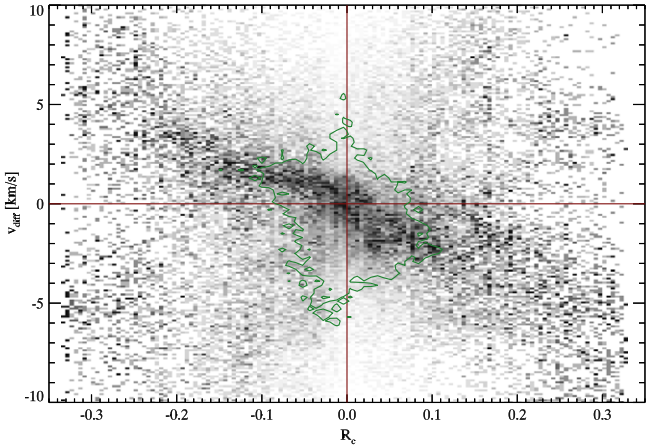

Figure 11. PDF of the velocity difference between the core and the peak formation heights (Equation (7)) as a function of the line asymmetry (Equation (6)). Red lines indicate $R_c = 0$ and $v_{\rm diff} = 0$.

formation height) above the peak formation height (negative $v_{\rm diff}$).

5.2. Line Shifts

Velocities along the line of sight in the atmosphere will cause a Doppler shift of the atomic absorption profile. If the velocity does not vary too much across the formation region of the intensity, we also get a corresponding Doppler shift of the intensity profile. Here, we will look at the correlations between the velocities in the atmosphere and the line core Doppler shift, the possible usage of the difference in Doppler shift between the two main C II lines to diagnose velocity gradients and finally the usage of a Gaussian fit to the whole line profile as a velocity diagnostic.

5.2.1. Doppler Shift of the Line Core

By choosing the line core as defined in Section 4.2, we have the hope of getting a diagnostic of the velocity in the atmosphere close to the transition region. Figure 12 shows the correlation of the Doppler shift of the line core and the line-of-sight velocity at the formation height of the intensity at that wavelength ($Z_{\rm fm}$ in Equation (5)).

Figure 12 shows that there is a good correlation between the vertical component of the velocity at the formation height and the Doppler shift of the line core. What appears as a bad correlation at the extreme ranges only concerns a small number of cases. The green contour and the Pearson correlation coefficient show that more than 50% of the points have a tight correlation.

An interesting feature can be seen in the right panel of Figure 12: a dark patch on the blueward side (positive Δv) for the C II 133.5 nm line along a line parallel to the $y = x$ line. These pixels represent columns where the core finding algorithm has found the blend at 133.566 nm instead of the main component. The blend is at a wavelength corresponding to a blueshift of 9 km s^{-1}. The other bands on either side of the $y = x$ line (and on the blue side of the band caused by the blend at 133.566 nm) for large absolute values of Δv represent columns where the core-finding algorithm has picked out the blue or red peak as the line core. This may happen when there are large velocity gradients smearing out the central depression

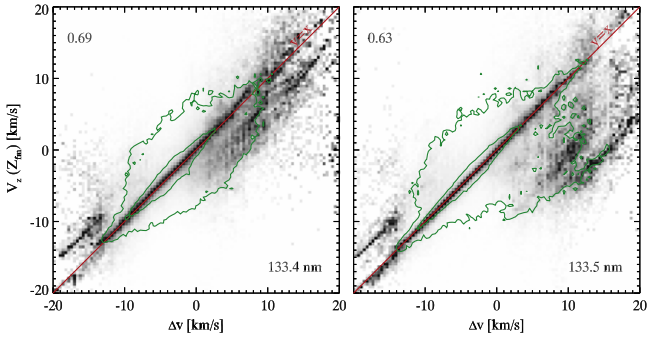

Figure 12. PDF of the line-of-sight velocity as a function of Doppler shift of the line core. The velocity is at the intensity formation height (Equation (5)) of the core wavelength. Positive velocity is upflow (blueshift). The line core is defined as in Section 4.2. The green contours encompass 50% and 90% of all points. Each column in the panels is scaled to maximum contrast to increase visibility. The Pearson correlation coefficient is given in the upper left corner. The red line denotes the line $y = x$.

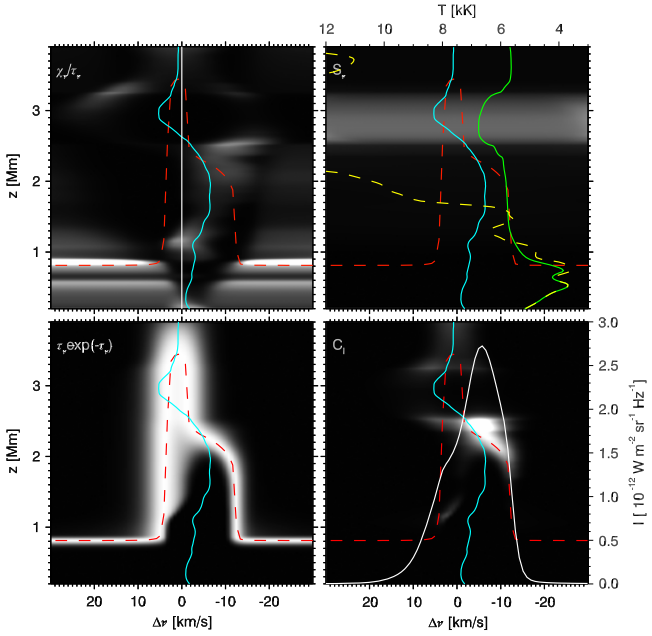

Figure 13. Contribution function to the intensity of the C II 133.4 nm line showing an example of an outlier. Each grayscale image shows the quantity specified in its top left corner as a function of frequency from line center (in Doppler shift units) and atmospheric height z. Multiplication of the first three produces the contribution function to specific intensity shown in the lower right panel. A $\tau_\nu = 1$ curve (red dashed) and the vertical velocity (blue solid, positive is upflow) are shown in each panel, with a $v_z = 0$ line in the upper left panel for reference. The image in the upper right panel is the total source function with lines showing the Planck function (yellow dashed) and the line source function (green solid) in radiation temperature units specified along the top. The lower right panel also contains the emergent intensity profile (white solid), with the scale along the right-hand side.

such that what is really a double-peak profile appears as a very asymmetric single-peak profile.

An example of an outlier is shown in Figure 13. At this column of the atmosphere, there is a strong velocity gradient. An upward velocity at 3 Mm height moves the atomic absorption profile to the blue and a downflow at 2 Mm moves the profile to the red. This creates a $\tau_\nu = 1$ (lower left panel) graph with a narrow peak at 3.5 Mm and a shoulder toward the red at 2–2.5 Mm. The contribution function to intensity is maximum at 2.5 Mm (lower right panel) but with a maximum

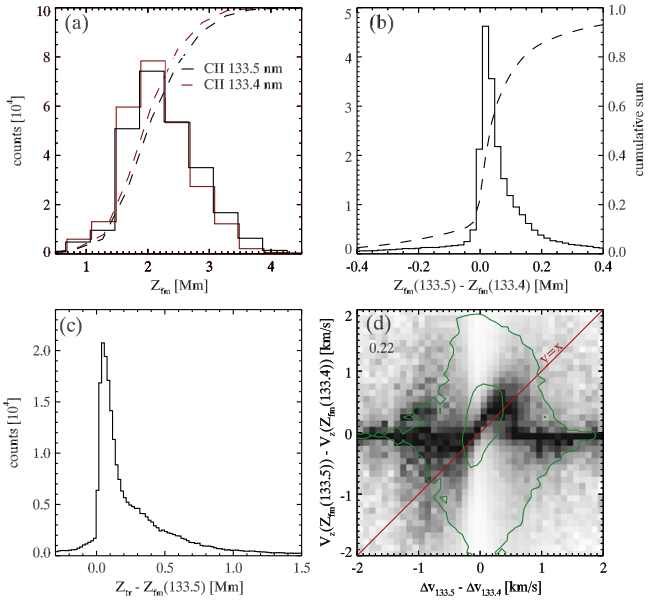

Figure 14. Different properties of the formation height ($Z_{\rm fm}$ in Equation (5)) of the C II 133.4 nm and C II 133.5 nm line cores (as found by the core finding algorithm). Histogram of formation height for both lines, (panel (a), C II 133.4 nm (red) and C II 133.5 nm (black)). Histogram of the difference between the formation heights of the lines (panel (b)). The cumulative sum of the histogram is shown with a dashed curve with the scale on the right hand side. Histogram of the difference between the transition region height and the formation height of the strongest line (panel (c)). PDF of the difference of the line-of-sight velocity at the formation height as a function of the difference in Doppler shift of the line cores (panel (d)). Each column is scaled to maximum contrast to increase visibility. The Pearson correlation coefficient for the data in the $[-0.5, 0.5]$ interval in x is given in the upper left corner. The red line denotes the line $y = x$. The green contours encompass 50% and 90% of all points.

on the red side of the velocity curve because of the gradient term χ_ν/τ_ν (upper left panel). Our algorithm picks out the maximum intensity wavelength (which has a redshift of $5\,{\rm km\,s^{-1}}$) as the line core (since this is a single-peak profile) although the wavelength where the optical depth unity is the highest is at zero shift. The velocity we measure ($5\,{\rm km\,s^{-1}}$) is also $2\,{\rm km\,s^{-1}}$ larger than the actual down flow at the formation height at this wavelength. The strong velocity gradient is the cause of both of these effects. With zero velocity, we would get a much narrower intensity profile with two intensity peaks where optical depth unity is coinciding with the source function maximum at 2.8 Mm and a central reversal with the intensity formed at the maximum height of unit optical depth of 3.5 Mm.

5.2.2. Combining Both Lines

Here we will discuss the possibility of using the lines together as a diagnostic of velocity gradients. The C II 133.5 nm line has 1.8 times the opacity of the C II 133.4 nm line and is thus formed higher up in the atmosphere. Figure 14 shows different properties for the formation of the two lines: histogram of the formation heights and the difference in formation height, formation height relative to the transition region, and finally the correlation between the difference in Doppler shift and the difference in velocity between the two formation heights.

The two line cores are formed close to the transition region (Figure 7) so the histogram in panel (a) of Figure 14 basically shows the distribution of the height of the transition region over the simulation columns. The C II 133.5 nm line is formed slightly higher than the C II 133.4 nm line, the peak of the distribution in panel (b) is at around 30 km. The opacity is a factor of 1.8 higher in the C II 133.5 nm line so optical depth unity is always higher by about 0.6 scale heights. However, the formation height shown in Figure 14 is weighted by the contribution function, and differences in the source function between the two lines may give a larger or smaller height difference than the expected 0.6 scale heights. Also, more importantly, the core finding algorithm may identify different wavelengths with respect to the rest wavelength as the core wavelength, especially in the presence of velocity gradients in the atmosphere and the presence of the blend on the blue side of the C II 133.5 nm line. These effects account for the small number of points with a negative height difference in panels (b) and (c) and also for the tail toward large height differences. The difference in Doppler shift of the cores of the two lines is correlated with the difference between the line-of-sight velocities at the respective formation heights when the Doppler shift difference is within $0.5\,{\rm km\,s^{-1}}$. Larger differences correspond to problems with the core algorithm and the correlation disappears.

5.2.3. Single Gaussian Fit Shift

Using the line core Doppler shift as a diagnostic of atmospheric velocities has the advantage that the line core is formed over a rather narrow height range compared with the intensity of the whole line. The diagnostic also provides a measure of the velocity in the uppermost chromosphere. The disadvantage is that sometimes the observationally determined line core is not really the part of the line that is formed in the highest region of the atmosphere. In noisy data there are also challenges in finding the number of peaks and the proper line core.

A common alternative is to use a Gaussian fit to the full line profile. The advantage is that all of the points in the profile are taken into account, thus minimizing the effect of noise. The disadvantage is that we get an influence on the shift from a much larger height range in the atmosphere. The profile may also deviate substantially from a Gaussian shape for a line formed under optically thick conditions or a line with a blend (like the C II 133.5 nm line). For a double-peak profile, one could devise a fitting with an emission Gaussian profile fitting the wings and a separate, absorption Gaussian, to fit the core. The additional fitting parameters demand a good signal-to-noise ratio to be robust. Therefore, here we test the simpler procedure of using a single Gaussian fit even for clearly non-Gaussian profiles (like double-peak ones) as a measure of the shift of the line. To overcome the bias toward the blue from the blend in the C II 133.5 nm line, we use the intensity averaged wavelength between the two components as the reference wavelength (133.57006 nm in this simulation) rather than the wavelength of the stronger component. Figure 15 shows that the shift from a single Gaussian fit is a good diagnostic of the atmospheric velocity at the height of unit optical depth.

An alternative to the single Gaussian fit is to use the first moment of the intensity with respect to wavelength. Again it is important to use the intensity weighted wavelength for the reference wavelength of the C II 133.5 nm line. Furthermore, the first moment measure is more sensitive to noisy data in the wings of the profile than the single Gaussian fit.

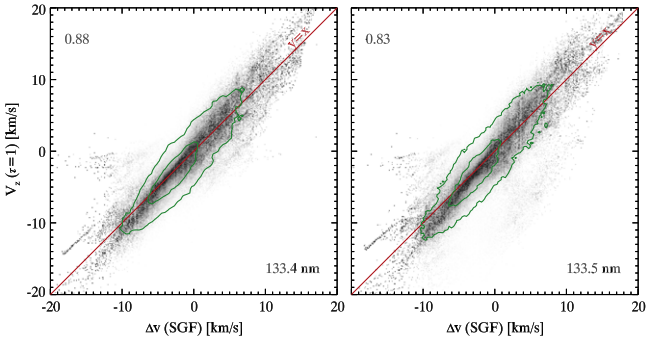

Figure 15. PDF of the line-of-sight velocity at the $\tau = 1$ height as a function of the single Gaussian fit shift for the C II 133.4 nm line (left panel) and the C II 133.5 nm line (right panel). The optical depth unity is taken at the wavelength of the Gaussian shift. The green contours encompass 50% and 90% of all points. Each column in the panels is scaled to maximum contrast to increase visibility. The Person correlation coefficient is given in the upper left corner. The red lines denote the line $y = x$.

5.3. Line Width

The width of the C II lines depends both on the width of the opacity profile (which is affected by the thermal width set by the temperature at the height of formation and by non-thermal motions) and by the variation of the source function between the height of formation of the continuum and the core of the line (see Paper I for a detailed discussion). We can characterize the width by several measures; the most common being the FWHM of the intensity profile, $W_{\rm FWHM}$, the standard deviation of a single Gaussian fit, σ, the half width at $1/e$ of the maximum intensity, ΔV_D (which is related to the most probable speed) and the second moment of the intensity with respect to wavelength relative to the first moment shift, W_2.

For a Gaussian intensity profile we have the following relations between the four width measures:

$$\Delta V_D = \sqrt{2}\,\sigma \tag{8}$$

$$W_{\rm FWHM} = 2\sqrt{\ln 2}\,\Delta V_D \tag{9}$$

$$W_2 = \sigma. \tag{10}$$

Figure 16 shows relations between various line-width characteristics for the C II 133.4 nm line. The upper left panel shows that the FWHM ($W_{\rm FWHM}$) is larger than Equation (9) applied to the $1/e$ width (ΔV_D) of a single Gaussian fit to the line profile (most points are above the red line). This implies that the line profiles, in general, have a "flatter top" than a Gaussian profile. This is of course true for the double-peak profiles that tend to be the broader ones. There are some points in the lower right part of the panel with small $W_{\rm FWHM}$ and large ΔV_D. These are very asymmetric double-peak profiles where one peak is less than half the intensity of the other such that the $W_{\rm FWHM}$ corresponds to the width of only the stronger peak while the single Gaussian fit is still affected by the full profile. The upper right panel of Figure 16 shows the relation between the measured width of the profile (given as $\sqrt{2}\,\sigma$ of a single Gaussian fit) and the non-thermal velocity in the line-forming region. The non-thermal velocity is defined as $\sqrt{2}$ times the rms of the line-of-sight velocities in the height range between optical depth unity in the continuum and the line core. As in the other correlation figures, we have the observable quantity on the x axis although the functional relationship is rather $x = f(y)$. The observed width is well correlated with the non-thermal velocities in the atmosphere, except for $\Delta V_D < 6$ km s^{-1}. These outliers correspond to profiles with a dominant optically thin component. The width is then dominated by the thermal width and the non-thermal velocities in a rather narrow formation region rather than in the full height range between the heights of optical depth unity in the continuum and the line core. The lower left panel of Figure 16 shows a histogram of the non-thermal velocities. The maximum of the distribution is close to 2 km s^{-1}, which is a rather small value. This will be further discussed in Section 8. The lower right panel of Figure 16 shows the "opacity broadening factor" defined from

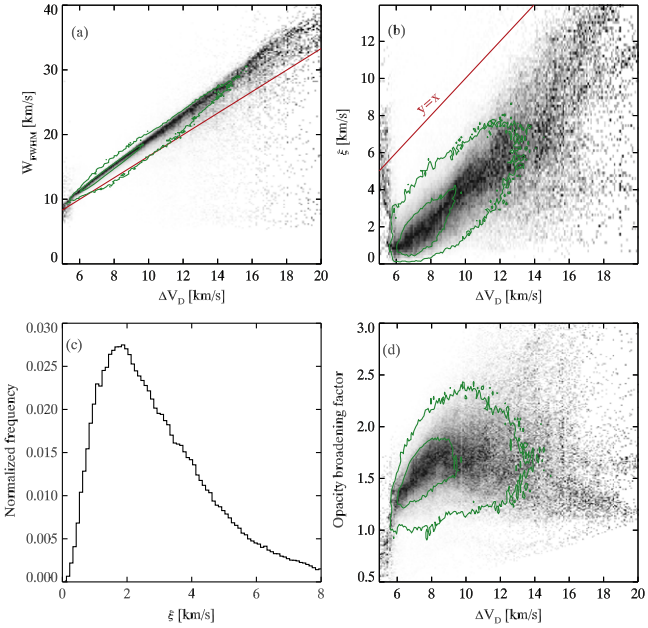

Figure 16. Relations between line-width characteristics: panel (a): PDF of $W_{\rm FWHM}$ as a function of ΔV_D of a single Gaussian fit. The red line shows the relation for a Gaussian intensity profile. Panel (b): PDF of the non-thermal velocity, ξ, as a function of ΔV_D of a single Gaussian fit. Panel (c): histogram of non-thermal velocities. Panel (d): PDF of opacity broadening factor as function of ΔV_D of a single Gaussian fit. The non-thermal velocity is taken as $\sqrt{2}$ times the rms of the line of sight velocities in the height range between optical depth unity in the continuum and the line core. The green contours encompass 50% and 90% of all points. Each column in the PDF panels is scaled to maximum contrast to increase visibility. All correlations are for the C II 133.4 nm line.

$$\text{Opacity broadening factor} = \frac{W_{\rm FWHM}}{2\sqrt{\ln 2}\sqrt{\dfrac{2kT}{m} + \xi^2}} \tag{11}$$

where T is the weighted average of the temperature over the line-forming region using the contribution function to total intensity as weighting function, m is the mass of carbon, and ξ is the non-thermal velocity defined above.

The non-thermal velocities as defined here give a contribution both to the width of the opacity profile (when the length scale of the velocity variations is small compared with the line-forming length scale; classical micro turbulence) and to shifts of the profile (for large length scales; classical macroturbulence). We can thus expect the opacity broadening as defined here to be lower than the effect discussed in Paper I and it may even be below one (which is the case for only very few points in Figure 16). The opacity broadening is mainly around a factor of 1.5, is smallest for the narrowest profiles (otherwise they

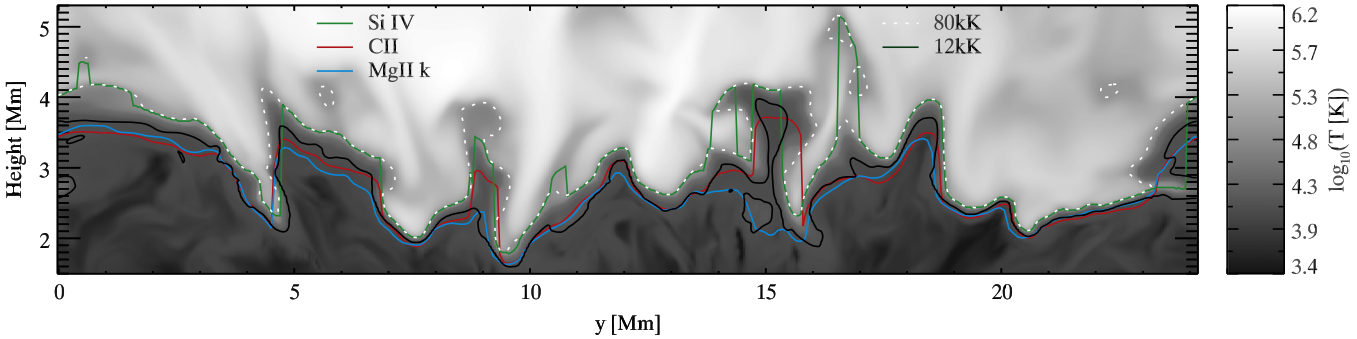

Figure 17. Formation height of the C II 133.5 nm line, the Mg II k line and the Si IV 139.3 nm line for the snapshot cutout at $x = 12$ Mm shown in Figure 1. Temperature on a logarithmic scale is shown as a grayscale image with contours at 80 kK (white dotted) and 12 kK (black). Maximum $\tau = 1$ heights are shown for the C II 133.5 nm line (red) and for the Mg II k line (blue) and the maximum emissivity height is shown for the Si IV 139.3 nm line (green).

would not be that narrow) and bifurcates into large and small values for the broadest profiles.

6. COMPARISON WITH OTHER *IRIS* SPECTRAL LINES

In Figure 17, we compare the formation heights of the C II 133.5 nm line, the Mg II k line and the Si IV 139.3 nm line for the snapshot cutout at $x = 12$ Mm shown in Figure 1. As formation height, we use the maximum $\tau = 1$ height for the C II and Mg II k lines and, for Si IV, we use the height of maximum emissivity as calculated from CHIANTI. This comparison shows that the Si IV line normally has the highest formation height at a temperature around 80 kK with the C II line and Mg II k line formed lower. The C II line is at some locations formed at a lower height than the Mg II k line (e.g., for $y = 0 - 4$ Mm) but often higher.

We show the formation heights of the C II 133.5 nm and the Mg II k lines in the whole box in Figure 18. The small patches of very high formation height for the C II 133.4 nm line (e.g., at $(x, y) = (11, 12)$ Mm) are caused by cooler pockets of plasma at large heights that have enough density to place $\tau = 1$ there. However, the temperature is not low enough in these bubbles for Mg II k to reach optical depth unity. From the figure, it is clear that the C II 133.5 nm and Mg II k formation heights show very similar patterns but that the C II line is formed higher up in the fibrils in the central part of the simulation domain (e.g., at $y = 15$ Mm), see also Figure 17.

The line opacity per unit mass is given by

$$\kappa_\nu^l = \frac{\pi e^2}{m_e c^2} n_l f_{lu} \phi_\nu \frac{1}{\rho} \tag{12}$$

where e is the electron charge (in e.s.u), m_e is the electron mass, c is the speed of light, n_l is the population density of the lower level, f_{lu} is the absorption oscillator strength, ϕ_ν is the atomic absorption profile, and ρ is the mass density. Here, we have neglected stimulated emission. Assuming a Doppler absorption profile (which is a good approximation at the line core forming region for these lines), we get for the opacity at line center for a spectral line of a singly ionized state:

$$\kappa_{\nu_0}^l = 0.02654 \frac{n_l}{N_{II}} \frac{N_{II}}{N_{el}} \frac{N_{el}}{N_H} \frac{N_H}{\rho} f_{lu} \frac{1}{\sqrt{\pi}\,\Delta\nu_D} \tag{13}$$

where N_{II} is the number density of the singly ionized state, N_{el} is the number density of the element, N_H is the number density of hydrogen particles, and $\Delta\nu_D$ is the $1/e$ width of the atomic absorption Doppler profile (in frequency units). The four

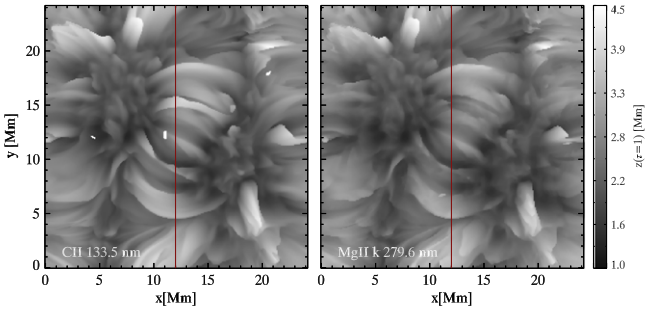

Figure 18. Maximum height of unit optical depth over the line profile for the C II 133.5 nm (left) and Mg II k (right) lines. The location of the cutout shown in Figure 17 is shown with a red line at $x = 12$ Mm.

population ratios are the fraction of the singly ionized state that is in the lower level of the transition (4/6 for the C II 133.5 nm line, 1 for the Mg II k line), the ionization fraction of the singly ionized state, the abundance of the element and the number of hydrogen particles per unit mass (a constant only dependent on the abundances), respectively. The $1/e$ width is given by

$$\Delta\nu_D = \frac{1}{\lambda_0}\sqrt{\frac{2kT}{m} + \xi^2}. \tag{14}$$

The abundance of carbon is a factor of 6.8 larger than that of magnesium (Asplund et al. 2009) while the oscillator strength is a factor of 5.2 higher for Mg II k. The thermal broadening is a factor of 1.4 larger for carbon (due to a factor of two lower mass). Inserting these numbers into Equation (13), and assuming identical ionization fractions for a moment, we find an opacity that is a factor of 3.4 larger for the Mg II k line if thermal broadening dominates $\Delta\nu_D$ and a factor of 2.4 larger if the non-thermal broadening dominates. Integrating this equation from the corona and downwards, the ionization fraction becomes critical. When the temperature drops below 50 kK we start to get substantial amounts of C II (10% ionization fraction at this temperature, see Paper I) while we still have negligible amounts of Mg II. The optical depth starts to increase for the C II 133.5 nm line while the Mg II k line still has negligible optical depth. At a temperature of 16 kK, we have 10% Mg II (Carlsson & Leenaarts 2012) and almost 100% C II. At a temperature lower than 14 kK, the optical depth builds up faster in the Mg II k line than in the C II 133.5 nm line because of the larger opacity factor estimated above and because carbon gets neutral below 8 kK while magnesium stays mostly in the singly ionized state to much lower temperatures. The C II 133.5 nm

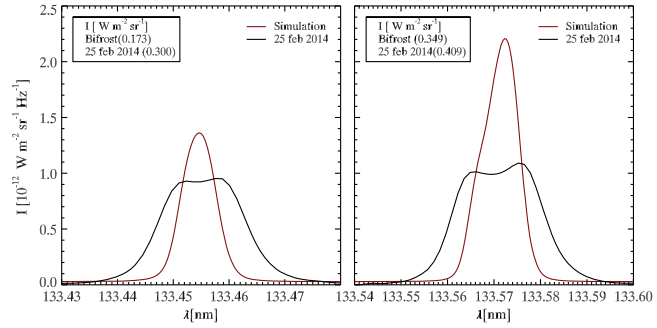

Figure 19. C II average line profiles from a quiet-Sun internetwork region observed on 2014 February 25 at 20:50 UT with the *IRIS* satellite (black) compared with the average spectral profiles from our *Bifrost* simulation snapshot (red). The simulation profiles have been convolved with the *IRIS* spectral resolution. The total intensity is given in the upper left corner.

line reaches optical depth unity at a greater height than the Mg II k line if there is a sufficient amount of material in the 14–50 kK temperature range, otherwise the Mg II k line is formed higher. Both cases are present in our *Bifrost* simulation as is evident from Figures 17 to 18. Velocity gradients will complicate this picture since the Mg II k line has a smaller thermal width and the opacity is therefore more sensitive to velocity gradients. This is seen in Figure 18 as locally smoother $\tau = 1$ surfaces for the C II 133.5 nm line than for the Mg II k line.

7. COMPARISON WITH OBSERVATIONS

The main purpose of this paper is to explore the diagnostic potential of the C II 133.4 nm and C II 133.5 nm lines. For that purpose, we have used a *Bifrost* simulation cube to map how atmospheric parameters are encoded in observable quantities. A comparison between the synthetic observables and observations will furthermore give information on what might be missing in the simulations for a realistic description of the solar atmosphere. It is important to stress, however, that we are not dependent on an accurate match between the synthetic observables and observations for the derived mapping of atmospheric parameters and observables to be relevant; it is enough that the simulation cube spans a relevant parameter range.

For this comparison, we use observations from the *IRIS* satellite taken on 2014 February 25 at 20:50 UT. This is a very large dense raster with 400 raster steps of 0.″35 with a spatial sampling of 0.″16 along the slit. The exposure time was 30 s for each raster step with 31.7 s step cadence and there is no binning in space or wavelength. The raster covers a field of view of $141'' \times 174''$ centered at $(x, y) = (-73'', 75'')$ and it took 3.5 hours to complete. The area observed corresponds to quiet Sun.

We have used *IRIS* calibrated level 2 and level 3 data, details of the data reduction are given in De Pontieu et al. (2014). The mean intensity profile of the quiet Sun internetwork region is shown in Figure 19. The total intensity summed over both lines is $0.71\,\mathrm{W\,m^{-2}\,sr^{-1}}$ in the observations, which should be compared with $0.52\,\mathrm{W\,m^{-2}\,sr^{-1}}$ that we get from the simulation cube and 0.42 and $0.87\,\mathrm{W\,m^{-2}\,sr^{-1}}$ from the two SUMER data sets reported by Judge et al. (2003).

While the total intensity of the two lines is similar between the simulation and the observations, there are some major differences. The simulations give a single-peak profile while the observations show a double-peak, much broader, profile.

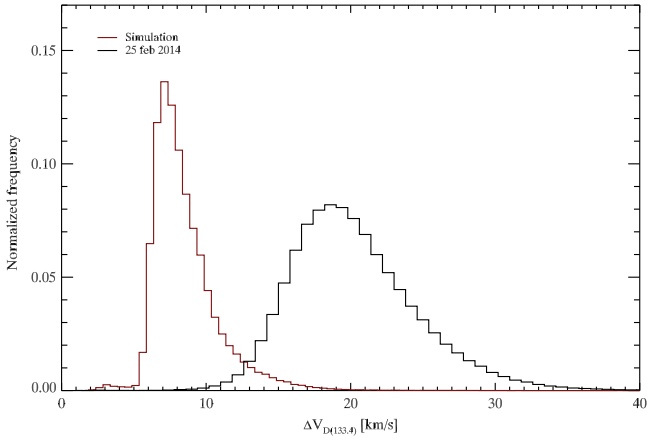

Figure 20. Histogram of ΔV_D for a single Gaussian fit for the C II 133.4 nm line in the simulation (red) and quiet solar internetwork region observation (black). The *IRIS* instrumental broadening has been removed from the observed values.

The ratio between the peak intensities is on average 1.4–1.6 in the simulation and 1.1–1.2 in the observations. This discrepancy is there not only for the mean profile but also for individual profiles. About 40% of the observed C II 133.4 nm quiet-Sun profiles are single-peak while we have 75% single-peak profiles in the simulation (Figure 3). The mean profiles in the observations have an asymmetry with the red peak stronger than the blue peak. This is opposite of what is the case for the Mg II h and k profiles (Leenaarts et al. 2013b). We speculate that this is caused by the fact that the formation of the C II peak happens mostly above the location where the gas pressure is equal to the magnetic pressure ($\beta = 1$ surface) in the internetwork while the Mg II h and k peaks are formed below. The Mg II h and k lines, therefore, get enhanced blue peaks from acoustic shocks and the C II lines do not. This is consistent with the visibility of internetwork chromospheric bright grains observed with *IRIS* (Martínez-Sykora et al. 2015).

Figure 20 gives the distribution of the profile widths in the simulation and in the quiet-Sun observational data set for the C II 133.4 nm line. The average width in the observations is $21\,\mathrm{km\,s^{-1}}$, more than twice the average width of $9\,\mathrm{km\,s^{-1}}$ we have in the simulation. However, the simulations show a similar *range* in widths with more than 200 profiles wider than $24\,\mathrm{km\,s^{-1}}$. We discuss possible reasons for the discrepancies between the simulations and the observations in Section 8.

8. DISCUSSION AND CONCLUSIONS

We have studied the diagnostic potential of the C II 133.4 nm and the C II 133.5 nm lines that are among the strongest lines in the FUV passbands of the *IRIS* spacecraft.

We found that local maxima in the source function between the formation height of the continuum and the line core can give rise to a variety of profile shapes. In the simulation, single-peak emission profiles dominate but there are also double and multiple peak profiles. Velocity gradients alter the shape expected from just the source function variation. We introduced an observational definition of the line core by taking the position of the central peak for profiles with an odd number of peaks and the position of the central depression for profiles with an even number of peaks. This definition in most cases gives a good approximation to the theoretical definition of the line core (the wavelength where the optical depth unity point is

the highest). However, in the presence of strong velocity gradients, we may get a filling in of the central reversal and incorrectly assign one of the peaks as the line core wavelength. The contribution to the line core intensity has its maximum close to the transition region (defined as being the highest height where the temperature is below 30 kK). The contribution function to intensity on a logarithmic optical depth scale shows that the dominant formation is optically thick with occasionally an optically thin component when the source function increases very strongly into the transition region.

We inspected various relations between atmospheric properties and observables. We found that the low intensity profiles tend to have a higher formation height. This means that the source function is lower at the formation height when the transition region is at a greater height. The intensity at the line core is only weakly correlated with the temperature at the formation height. Normally, the source function has decoupled from the Planck function at this height such that the actual temperature at the formation height is about twice the radiation temperature of the line core intensity. There is a large scatter and the relation is of limited practical use.

The intensity ratio between the C II 133.5 nm and the C II 133.4 nm lines is 1.8 in the optically thin case and can be any value (including the optically thin value of 1.8) in the optically thick case depending on the ratio of the source functions of the two lines. This means that a value different from 1.8 shows optically thick formation while a value of 1.8 does not prove optically thin conditions. The ratio of the peak intensities in the C II 133.5 nm lines in the *Bifrost* simulation snapshot is, on average, 1.4–1.7 with the lower value for double-peak profiles. Double-peak profiles often show an asymmetry with one peak brighter than the other. This asymmetry is correlated with the velocity gradient that exists between the formation height of the peaks and the line core. A blue peak that is stronger than the red peak means the atmosphere has a downflow at the core formation height relative to the motion at the formation height of the peaks.

The line core Doppler shift is well correlated with the line-of-sight velocity at the formation height. Due to the difficulties in observationally identifying the line core, there is substantial scatter in the relation. The blend on the blueward side of the C II 133.5 nm line also causes occasional misidentifications. The C II 133.4 nm line is formed some 30 km below the C II 133.5 nm line. The difference in Doppler shift between the two lines is correlated with the velocity gradient in this height interval. A single Gaussian fit to the whole profile is well correlated with the velocity at unity optical depth. Such a fit is easier to make in the presence of noise than using our core-finding algorithm that works best for observations with high signal-to-noise ratios.

The line width is well correlated with non-thermal velocities between the formation heights of the continuum and the line core. In addition to the width of the atomic absorption profile (which is affected by thermal and non-thermal motions), we get an additional broadening due to the optically thick line formation. This additional broadening, often called "opacity broadening," is an additional factor in the range 1.2–2, but sometimes reaching 4. The factor depends on the behavior of the source function between the formation heights of the continuum and the line core. For single-peak profiles with a source function that rises steeply into the transition region, the opacity broadening is small and, for source functions that rise rapidly in the lower chromosphere and then flatten out or decrease, the opacity broadening is large.

We compared the formation height of the C II 133.5 nm line with that of Mg II k and Si IV 139.3 nm. The Si IV line is formed the highest around 80 kK temperature while the C II and Mg II k lines are formed lower at similar heights below the transition region. The relative formation height of the two lines depend on the amount of matter in the 14–50 kK temperature range. With significant amounts of matter in this temperature range where magnesium is still more than singly ionized, the C II 133.5 nm line is formed above the Mg II k line but, with less material in this temperature range, we have the opposite situation.

We compared the simulation results with recent observations from *IRIS*. The total intensity of the mean profiles from the simulations is in general agreement with the observed values but the observed profiles are a factor of 2.5 wider than the ones in the simulation. Also, the observed intensity ratio between the C II 133.5 nm and C II 133.4 nm lines ranges between 1.1 and 1.2, compared to the range 1.4–1.7 found in our simulations. The mean profile from the simulations is single peaked while in observations of the quiet Sun, the mean profile is double peaked. There is also a larger proportion of single-peak profiles in the simulations than in the observations.

Double-peak profiles come from the existence of a local source function maximum between the formation heights of the continuum and the line core caused by a temperature rise and sufficient coupling between the Planck function and the source function. This means that we have too low temperatures in the low-mid chromosphere in the simulation compared with what observations of the quiet-Sun reveal. Increasing the number of double-peak profiles through increased heating in the lower chromosphere in the simulation would also increase the width through increased opacity broadening. In addition, this comparison shows that we have too small non-thermal velocities in the middle chromosphere in the simulations.

All the correlations have been derived with the full spectral and spatial resolution of the *Bifrost* simulation. At *IRIS* resolution, we still expect most of the results to be valid. Convolving our intensity profiles with the *IRIS* resolution decreases the proportion of double-peak C II 133.5 nm profiles from 23% to 9%, which further increases the disproportion of single-peak over double-peak profiles in our simulations compared to observations. However, we expect the effect on the solar profiles to be much smaller since our synthetic profiles are too narrow by a factor of two. The correlation between Doppler shift differences and velocity differences between the two C II lines was only significant for Doppler shift differences smaller than $0.5\,\mathrm{km\,s^{-1}}$. Measuring Doppler shifts to that precision with the *IRIS* spectral pixels of $2.9\,\mathrm{km\,s^{-1}}$ is possible, but requires a high signal-to-noise ratio.

Although there are large differences between the mean properties of the synthetic profiles and the observations, we find that the simulations cover most of the parameter range shown by the observations of the quiet-Sun (although in very different distributions). We thus believe the derived relations are valid under solar conditions. The mere fact that there are large differences in the distribution of properties between the synthetic profiles and the observed ones shows that the C II 133.4 nm and C II 133.5 nm lines are powerful diagnostics of the chromosphere and lower transition region.

The research leading to these results has received funding from the European Research Council under the European Union's Seventh Framework Programme (FP7/2007-2013)/ERC grant agreement No. 291058. This research was supported by the Research Council of Norway through the grant Solar Atmospheric Modelling and through grants of computing time from the Programme for Supercomputing and through computing project s1061 from the High End Computing Division of NASA. B.D.P. acknowledges support from NASA grants NNX11AN98G and NNM12AB40P and NASA contract NNG09FA40C (*IRIS*).

REFERENCES

Asplund, M., Grevesse, N., Sauval, A. J., & Scott, P. 2009, ARA&A, 47, 481
Carlsson, M., & Leenaarts, J. 2012, A&A, 539, A39
de la Cruz Rodríguez, J., De Pontieu, B., Carlsson, M., & Rouppe van der Voort, L. H. M. 2013, ApJL, 764, L11
De Pontieu, B., Title, A. M., Lemen, J. R., et al. 2014, SoPh, 289, 2733
Gudiksen, B. V., Carlsson, M., Hansteen, V. H., et al. 2011, A&A, 531, A154
Gustafsson, B. 1973, UppAn, 5, 6
Hummer, D. G., & Voels, S. A. 1988, A&A, 192, 279
Judge, P. G., Carlsson, M., & Stein, R. F. 2003, ApJ, 597, 1158
Leenaarts, J., & Carlsson, M. 2009, in ASP Conf. Ser. 415, The Second Hinode Science Meeting: Beyond Discovery-Toward Understanding, ed. B. Lites et al. (San Francisco, CA: ASP), 87
Leenaarts, J., Carlsson, M., & Rouppe van der Voort, L. 2012, ApJ, 749, 136
Leenaarts, J., Pereira, T. M. D., Carlsson, M., Uitenbroek, H., & De Pontieu, B. 2013a, ApJ, 772, 89
Leenaarts, J., Pereira, T. M. D., Carlsson, M., Uitenbroek, H., & De Pontieu, B. 2013b, ApJ, 772, 90
Martínez-Sykora, J., Rouppe van der Voort, L., Carlsson, M., et al. 2015, ApJ, 803, 44
Ng, K.-C. 1974, JChPh, 61, 2680
Olson, G. L., Auer, L. H., & Buchler, J. R. 1986, JQSRT, 35, 431
Pereira, T. M. D., Carlsson, M., de Pontieu, B., & Hansteen, V. 2015, arXiv:1504.01733
Pereira, T. M. D., Leenaarts, J., de Pontieu, B., Carlsson, M., & Uitenbroek, H. 2013, ApJ, 778, 143
Rathore, B., & Carlsson, M. 2015, ApJ, 811, 80
Rybicki, G. B., & Hummer, D. G. 1991, A&A, 245, 171
Rybicki, G. B., & Hummer, D. G. 1992, A&A, 262, 209
Štěpán, J., Trujillo Bueno, J., Carlsson, M., & Leenaarts, J. 2012, ApJL, 758, L43